JOURNAL OF MATERIALS SCIENCE **31** (1996) 2317–2324

Crystallographic shear planes in nanocrystalline SnO_2 thin films by high-resolution transmission electron microscopy

J.G. ZHENG*[§], XIAOQING PAN[‡], M. SCHWEIZER[†], U. WEIMAR[†], W. GÖPEL[†], M. RÜHLE[‡]
National Laboratory of Solid State Microstructures in Nanjing University, Nanjing, People's Republic of China
[†]*Institute of Physical and Theoretical Chemistry, University of Tübingen, Auf der Morgenstelle 8, D-72076 Tübingen, Germany*
[‡]*Max-Planck Institut für Metallforschung, Institut für Werkstoffwissenschaft, Seestrasse 92, D-70174 Stuttgart, Germany*

Atomic structures of crystallographic shear planes (CSPs) in nanocrystalline thin films of semiconductor SnO_2 were investigated by high-resolution electron microscopy. The films were prepared by electron beam evaporation in high vacuum (10^{-6} torr) and followed by annealing in synthetic air at 700 °C for 1–2 h. CSPs with the displacement vector of $[\frac{1}{2}0\frac{1}{2}]$ were observed in the planes parallel to $(\bar{1}01)$, (110) and $(\bar{3}\bar{2}1)$. Most of the CPSs were found to terminate or interact with each other within SnO_2 crystallites. Partial dislocations exist at terminal places of CSPs or along intersecting lines of CSPs. CSP steps were also observed. Structural models of these defects have been proposed. Based on analysis of experimental data, it has been suggested that the Sn/O ratio at CSPs which are not parallel to their displacement vector, at cores of partial dislocations and at CSP steps, is higher than that of the perfect structure, that is, these defects are able to provide extra free electrons with the films.

1. Introduction

Cassiterite, SnO_2, is a wide band-gap metal oxide semiconductor having unique electronic and optical properties [1,2]. It is of considerable technological interest because of its applications in gas-sensing elements [3,4], in solar cells, as transparent electrodes and as a catalytic support material [5]. In recent years, scientists, stimulated by the discovery of novel properties of nano-particles [6,7] and by increasing demand for environmental protection, paid much attention to polycrystalline SnO_2 materials composed of nanometre-sized crystallites, especially, nanocrystalline SnO_2 films [8–12]. Nanocrystalline SnO_2 materials show better performance in detecting gases and different sensing mechanisms with respect to traditional materials. In contrast to extensive studies of electrical properties of these materials, a knowledge of their microstructures is within the limits of morphology [13]. So far, there have been no contributions to describe at an atomic scale defect structures of nanocrystalline SnO_2 materials. Defects in semiconductor SnO_2 can influence the density of charge carriers and subsequently material performance in detecting gases when this material is used as a sensing element. Thus the study on defect structures of semiconductor SnO_2 is of importance both academically and in application. The aim of the work was to determine atomic structures of crystallographic shear planes (CSPs) and further to provide useful information of local composition at these defects in nanocrystalline SnO_2 thin films.

In general, defect structures can be determined by a combination of conventional transmission electron microscopy (TEM) and high-resolution transmission electron microscopy (HRTEM). Because of small crystallite size and random orientations of crystallites, HRTEM becomes an exclusive but powerful technique to observe defects in the films. The improved resolution of HRTEM enables us to determine defect structure at an atomic scale [14].

2. Experimental procedure

Amorphous oxygen-deficient SnO_{2-x} thin films were prepared by electron-beam evaporation in high vacuum (10^{-6} torr; 1 torr = 133.322 pa) from high-purity SnO_2 (99.999%) on (1 0 0) surfaces of NaCl single crystals. Nanocrystalline SnO_2 films were

---

[§] *Present address*: H.H. Wills Physics Laboratory, University of Bristol, Tyndall Avenue, Bristol, BS8 1TL, UK

0022–2461

obtained by post-deposition annealing of the films in synthetic air at 700 °C for 1–2 h. For HRTEM observations, specimens were prepared by dissolving NaCl substrates in water and mounting the separated SnO_2 films on copper grids. Investigations were carried out in a Jeol JEM-4000EX microscope equipped with a Gatan slow-scan CCD camera, operating at 400 kV with a point-to-point resolution of 0.17 nm. The interpretation of observed micrographs is needed to compare them with simulated images. Image simulation was performed by use of a multislice method on the basis of dynamic scattering theory. The corresponding computer program pocket was kindly provided by Professor Y. M. Chu.

2.1. Idealization of cassiterite structure (SnO_2)

Cassiterite, SnO_2, has a rutile-type structure, as illustrated in Fig. 1a. Edge-shared $[SnO_6]$ octahedra form chains along *c*. Orientations of the octahedra in adjacent chains which are connected by corner-sharing differ by 90°. The unit cell outlined by broken lines is tetragonal ($a = 0.4737$ nm, $c = 0.3185$ nm) with tin atoms at $(0,0,0)$ and $(\frac{1}{2}a, \frac{1}{2}a, \frac{1}{2}c)$ and oxygen atoms at $\pm(ua, ua, 0)$ and $(\frac{1}{2}a, \frac{1}{2}a, \frac{1}{2}c) \pm (ua, -ua, 0)$, with $u = 0.307$ [15]. Fig. 1b shows the projection of SnO_2 along *b*, in which a projected unit cell is drawn. The stacking sequence of atomic (ionic) layers in one period along *b* is –O–Sn–O–Sn–⋯. This diagram suggests that oxygen atoms (anions) are approximately in hexagonal close-packed (h c p) arrangement and form an octahedral framework, and that metal atoms (cations) are sandwiched between oxygen layers and fill alternate rows of octahedral interstices in each interstice layer parallel to the (0 1 0) plane. Orientations of the rows are along the [0 0 1] direction. Arrangements of filled octahedral interstices or tin atoms are the same in each (0 1 0) Sn layer and tin atomic positions in adjacent tin layers are only shifted relatively by $\frac{1}{2}\langle 1\,1\,1 \rangle$. In Fig. 1b, three rows of octahedral interstices in one interstice layer at $y = 0$ are drawn: two rows are filled and one row is empty. Filled octahedra in adjacent layers are joined by corner-sharing. Empty octahedra in one layer connect filled octahedra in adjacent layers by face-sharing. Familiarity with the configuration of filled octahedra in a perfect crystal is helpful to understand defect structures because the difference between defect structures and perfect structure is in arrangements of the tin atoms without considering point defects in the oxygen sublattice.

It should be noted that in Fig. 1b, tin atoms are arranged flatly in (0 1 0) planes; however, oxygen atoms in (0 1 0) close-packed layers are slightly puckered. The puckering of (0 1 0) oxygen layers can be detected from projected heights of oxygen as shown in Fig. 1b. It is also indicated by heavy solid lines in the projection of SnO_2 along *c* (Fig. 1c). The puckering of oxygen layers results in a small difference between filled and empty octahedra. In order to visualize conveniently a derived defect structure, the oxygen sublattice structure is idealized by a small topological distortion in following diagrams.

Fig. 1d shows the projection of idealized SnO_2 along *c*. In contrast to Fig. 1c, the distortion flattens oxygen layers parallel to (0 1 0) and makes oxygen octahedra regular. The difference between filled and empty octahedra disappears in the idealized structure. Fig. 1e shows the (0 1 0) layer structure of idealized SnO_2, including only one oxygen layer and one tin layer. Positions of empty octahedral interstices are marked by " + ". The distortion generates a perfect h c p oxygen arrangement. The vector $\frac{1}{2}[1\,0\,1]$ is an exact oxygen–oxygen vector in idealized SnO_2. Patterns of occupied octahedral interstices in defect structures are different from the pattern in perfect SnO_2, that is, some filled octahedra in defect structures may correspond to empty ones in perfect SnO_2, and vice versa. Defect structures can be easily illustrated in the (0 1 0) layer structure by adding or deleting tin atoms at octahedral interstices or by displacing tin atoms from filled interstices to empty interstices on the basis of idealized SnO_2. However, the [0 1 0] direction (*b*) is obviously not the right direction to determine defect structures such as CSPs by use of HRTEM technique. Even if one empty interstice of perfect structure is occupied by a tin atom in a defect structure, one cannot identify this metal atom when observing the real crystal along *b* by HRTEM. The reason is that in the projection of SnO_2 along *b*, empty and filled interstices in (0 1 0) layers are superposed alternately. Fig. 1f presents the projection of idealized SnO_2 along $\langle 1\,1\,1 \rangle$. Broken lines outline unit cells viewed along the $[\bar{1}\,1\,\bar{1}]$ and $[1\,\bar{1}\,1]$ directions. Indices of lattice planes are marked which depend on viewing directions. One filled octahedron (A) and one empty octahedron (B) in the (0 1 0) layer at $y = 0$ are outlined. In the adjacent (0 1 0) layer at $y = 0.5$ they are outlined at C and D, respectively. Fig. 1f also shows positions of empty octahedral interstices which correspond to those marked by " + " in Fig. 1e. Filled octahedral interstices in adjacent (0 1 0) layers are superposed on each other in this diagram, as are empty octahedral interstices, that is, empty and filled interstices are separated in the projection of the structure along $\langle 1\,1\,1 \rangle$ directions. If an empty interstice of perfect SnO_2 is occupied by one tin atom, one can detect this atom when viewing the real crystal along $\langle 1\,1\,1 \rangle$ directions. Thus, $\langle 1\,1\,1 \rangle$ directions are appropriate directions to be used in determining defect structures by HRTEM.

3. Results and discussion

Nanocrystalline SnO_2 films of thickness about 8 nm are polycrystalline. They are composed of SnO_2 crystallites with diameters in the range 5–30 nm. CSPs in the crystallites were frequently observed in a high-resolution transmission electron microscope. The contrast of HRTEM images of SnO_2 mainly results from the tin sublattice because of the low scattering capacity of oxygen for incident electrons. Fig. 2a is the HRTEM image of a SnO_2 crystallite viewed along the $[\bar{1}\,1\,\bar{1}]$ direction. The image was taken under the defocus $\Delta f \approx -30$ nm which was measured by *in situ* Fourier transformation of amorphous SnO_2

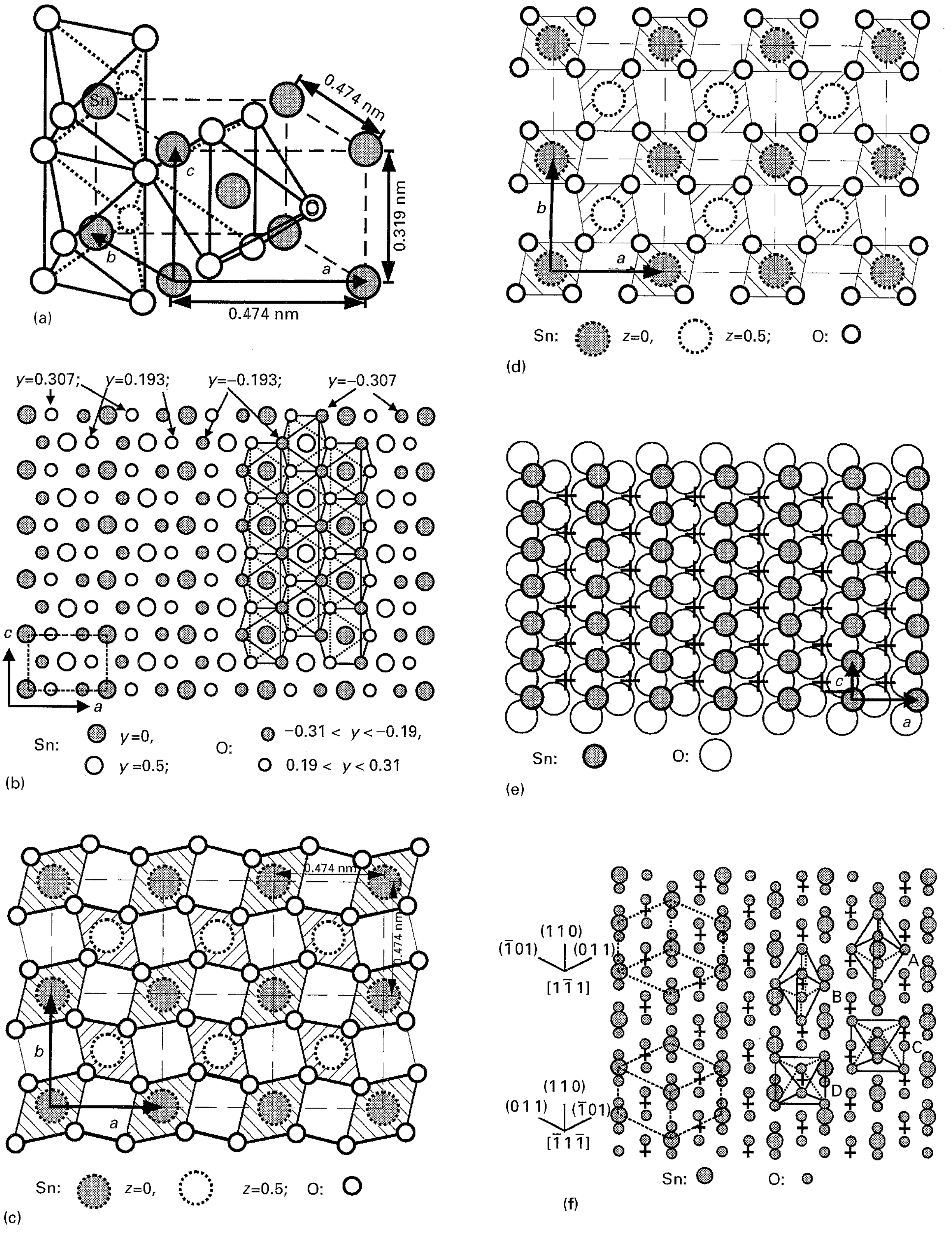

Figure 1 (a) Cassiterite SnO_2 structure. (b, c). The projection of cassiterite SnO_2 along the [0 1 0] and [0 0 1] directions, respectively. (d–f) Idealized SnO_2 projected along the [0 0 1] direction, illustrated in the (0 1 0) layer structure and projected along ⟨1 1 1⟩ directions, respectively.

existing in the edge of the sample. The inset shows a simulated image with parameters: defocus of the objective lens − 30 nm, crystal thickness 8 nm, accelerating voltage of electron 400 kV, spherical aberration coefficient $C_s = 1.0$ mm, defocus due to chromatic aberration − 6.4 nm, beam convergence 0.6 mrad, objective aperture radius 13.4 nm^{-1}. Image simulation suggests that black spots in Fig. 2a correspond to projections of tin atoms along the $[\bar{1}\,1\,\bar{1}]$ direction. A unit cell and characteristic lattice planes are marked on this HRTEM image and subsequent figures. Fig. 2a shows a CSP which is parallel to the $(\bar{1}\,0\,1)$ plane. Across the CSP there is a relative displacement of half (1 1 0) tin-lattice spacing. Compared with Fig. 1f, tin atoms on one side of the CSP are situated at octahedral interstices which are empty in the perfect structure. Fig. 2b gives the structural model of the CSP projected along the $[\bar{1}\,1\,\bar{1}]$ direction. Across the CSP, the distorted hcp net of oxygen continues, but tin nets are in antiphase, that is, filled and empty octahedral interstices are interchanged across the CSP. This characteristic is more clearly shown in the (0 1 0) layer structure of the CSP (Fig. 2c).

Across the CSP in Fig. 2c adjacent parts are relatively displaced towards one another by the vector $R = [\frac{1}{2}\,0\,\frac{1}{2}]$ (the displacement vector of the CSP). Fig. 2c shows that the density of metal atoms at the CSP is the same as that of a perfect crystal. In perfect SnO_2, the coordination number is 6 for a tin atom and 3 for an oxygen atom, and each $[SnO_6]$ octahedron

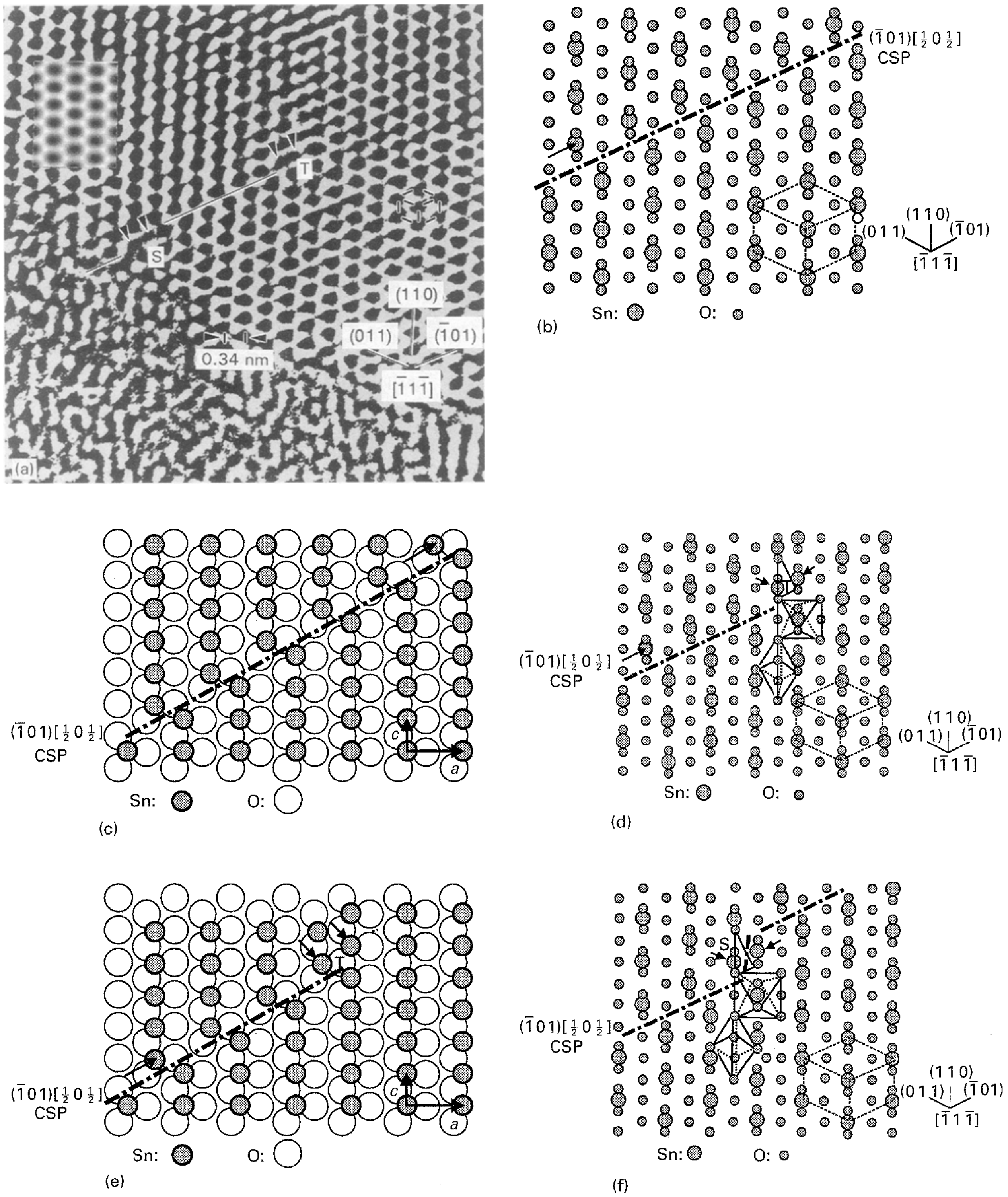

Figure 2 (a) HRTEM image of a SnO_2 crystallite taken at defocus − 30 nm along the $[\bar{1}\,1\,\bar{1}]$ direction, showing a $(\bar{1}\,0\,1)\,[\frac{1}{2}\,0\,\frac{1}{2}]$ CSP as well as a CSP step at S and a partial dislocation of Burgers vector $[\frac{1}{2}\,0\,\frac{1}{2}]$ at T. The inset is a simulated image with parameters as given in the text. (b, c) The structural model of the $(\bar{1}\,0\,1)\,[\frac{1}{2}\,0\,\frac{1}{2}]$ CSP projected along the $[\bar{1}\,1\,\bar{1}]$ direction, and illustrated in the (0 1 0) layer structure, respectively. (d, e) Core structure of the partial dislocation (at T) projected along the $[\bar{1}\,1\,\bar{1}]$ direction, and illustrated in the (0 1 0) layer structure, respectively. (f, g) Atomic arrangements of the CSP step (at S) projected along the $[\bar{1}\,1\,\bar{1}]$ direction, and illustrated in the (0 1 0) layer structure, respectively. (h) The pattern of oxygen vacancies required by the crystallographic shear of $[\frac{1}{2}\,0\,\frac{1}{2}]$ in order to produce a CSP step as shown in (g).

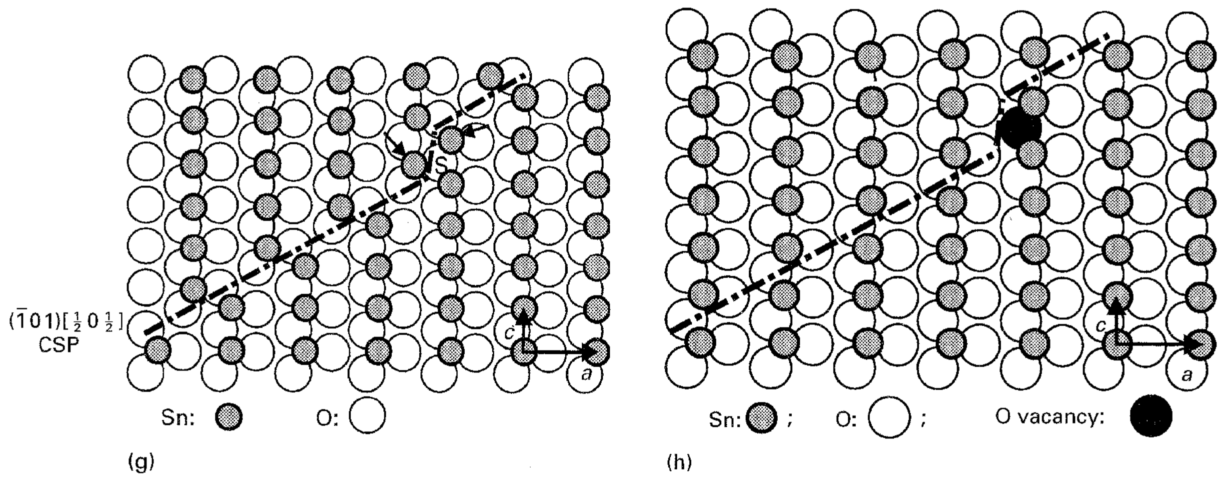

Fig. 2. continued

shares six vertices and two edges with its neighbours. At the CSP, the coordination number of tin and oxygen remains unchanged with respect to that in the perfect crystal, and each $[SnO_6]$ octahedron still shares six vertices and two edges with its neighbours, although relative positions of the filled octahedra are varied. Therefore, the Sn/O ratio at an infinite $(\bar{1}\,0\,1)$ CSP with $R = [\frac{1}{2}0\frac{1}{2}]$ is the same as that of perfect SnO_2, and the CSP does not provide extra free electrons with the films. A CSP passing through a crystallite can be regarded as an infinite CSP.

In fact, most of CSPs terminate within crystallites (Fig. 2a) or interact with each other (as shown below). At the terminal place of a CSP, marked by T in Fig. 2a, there is a partial dislocation with Burgers vector $[\frac{1}{2}0\frac{1}{2}]$, which equals to the displacement vector of the CSP. Fig. 2a clearly shows the tin arrangements at the core (T) of the partial dislocation. The line direction of the dislocation is judged from the image to be approximately parallel to the $[\bar{1}\,1\,\bar{1}]$ direction. The distance between two tin atomic columns marked at T is equals to about half of a normal distance. Away from the core for a few nanometres, tin atomic columns have approximately normal distance between them. Fig. 2d shows a model of core structure of the partial dislocation projected along the $[\bar{1}\,1\,\bar{1}]$ direction. Compared with Fig. 1e, tin atoms belonging to two marked columns at T occupy octahedral interstices which are the filled and empty sites in perfect structure, respectively. The filled and empty octahedra in perfect structure are joined by face-sharing. Two octahedra, which are joined by face-sharing at T, and a common face of these two octahedra are outlined. Thus, there are pairs of face-shared octahedra arranged along the dislocation line. The pair is oriented parallel to the $[0\,1\,0]$ direction. Fig. 2e shows the $(0\,1\,0)$ layer structure of the core of the partial dislocation. The octahedron containing the tin atom at T (on the left) connects a $[SnO_6]$ octahedron in a lower adjacent layer by face-sharing. The orientation of the pair of octahedra is parallel to the normal line. Fig. 2e shows that the density of tin atoms at the core of the partial dislocation is higher than that of the perfect structure, while the oxygen density is the same as that of the perfect structure. This means that the Sn/O ratio at the core is higher than that in the perfect structure, and the core of the partial dislocation is capable of providing extra free electrons with the films.

The structural model of a CSP in SnO_2 can be deduced from the idealized perfect structure by a geometrical operation $(h\,k\,l)$ $[u\,v\,w]$. The idealized perfect structure is cut into two parts at the $(h\,k\,l)$ plane which are then displaced relatively by the vector $[u\,v\,w]$, and then connected. Then, a CSP parallel to the (hkl) plane with displacement vector $[u\,v\,w]$ is obtained. When (hkl) is not parallel to $[u\,v\,w]$, some atoms should be eliminated from the perfect structure so that the operation does not lead to superposed atoms. The operation is valid for describing the structure of a CSP whether or not it is the actual mechanism by which crystallographic shear occurs in a crystal. The CSP in Fig. 2c can be produced by applying a geometric operation of $(\bar{1}\,0\,1)$ $[\frac{1}{2}0\frac{1}{2}]$ to Fig. 1e. The operation of $(\bar{1}\,0\,1)$ $[\frac{1}{2}0\frac{1}{2}]$ is allowed without eliminating any oxygen from Fig. 1e because the displacement vector of the CSP is parallel to the orientation of the CSP. This also reveals that the composition at the $(\bar{1}\,0\,1)$ $[\frac{1}{2}0\frac{1}{2}]$ CSP is the same as that of perfect SnO_2.

When the orientation of a CSP deviates from the $(\bar{1}\,0\,1)$ plane, that is, the displacement vector of a CSP is no longer parallel to the orientation of the CSP, the composition at this CSP is different from that of perfect SnO_2. A step at the $(\bar{1}\,0\,1)$ $[\frac{1}{2}0\frac{1}{2}]$ CSP can be regarded as such a local CSP. Fig. 2a shows an example of a CSP step at S. The step is oriented parallel to the $[\bar{1}\,1\,\bar{1}]$ direction. Two tin atomic columns marked at S have a much shorter distance which is about half of a normal distance. Fig. 2f shows the structural model of the CSP step projected along the $[\bar{1}\,1\,\bar{1}]$ direction. Tin atoms of the two marked columns fill pairs of face-shared octahedra. A pair of octahedra, which are joined by face-sharing at the CSP step and a common face of the octahedral pair are outlined. The $(0\,1\,0)$ structure of the step is shown in Fig. 2g. The octahedron containing the tin atom indicated on the left at S shares a face with a $[SnO_6]$ octahedron in the lower adjacent layer. This is similar to the situation shown at the core of the partial dislocation at T (Fig. 2e). The step can be generated by a crystallographic shear of displacement vector

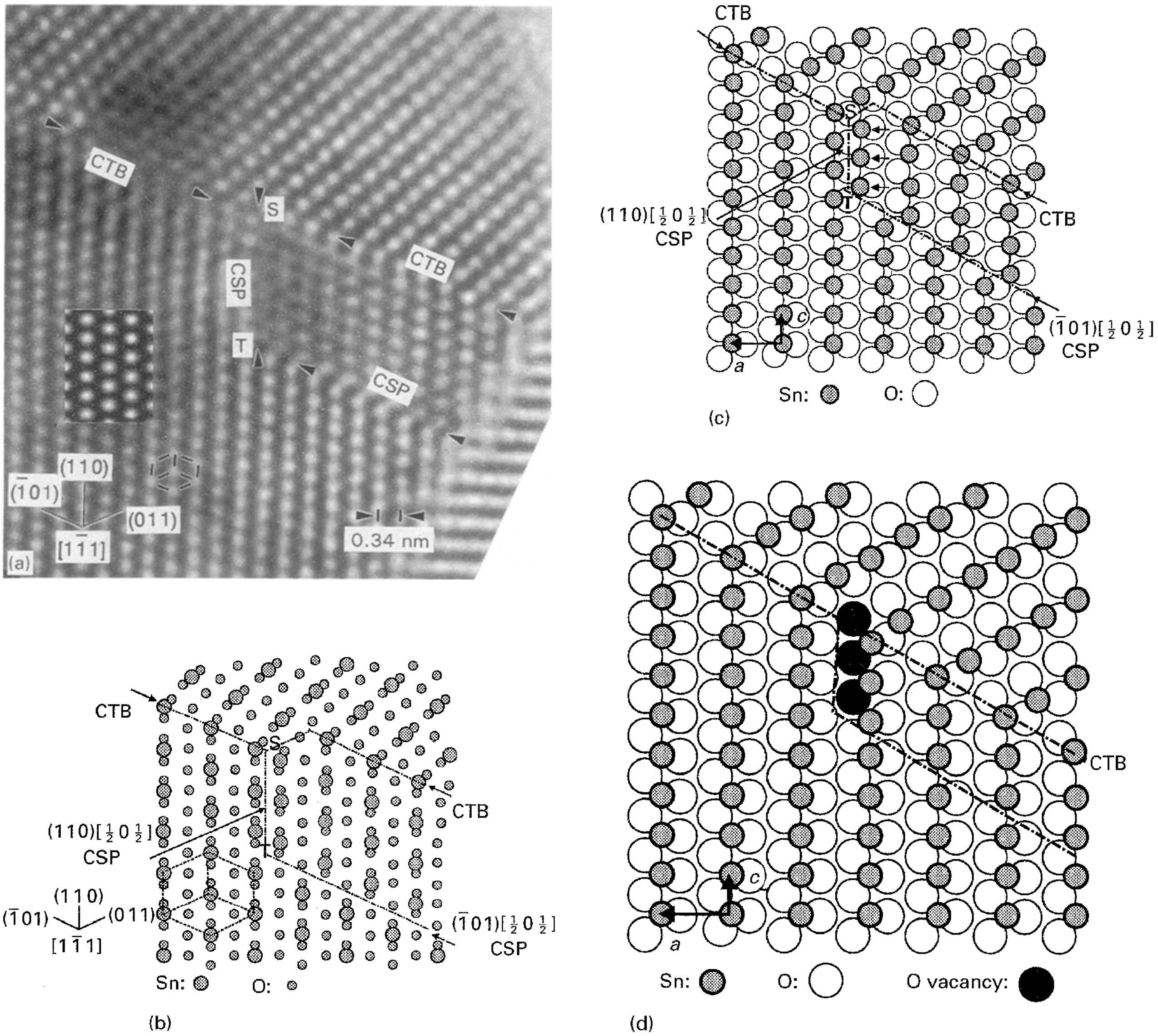

Figure 3 (a) HRTEM image of a SnO_2 crystallite taken at defocus − 10 nm along the $[1\bar{1}1]$ direction, showing a $(1\,1\,0)\,[\frac{1}{2}0\frac{1}{2}]$ CSP between S and T as well as a $(\bar{1}\,0\,1)\,[\frac{1}{2}0\frac{1}{2}]$ CSP and a CTB parallel to the $(\bar{1}\,0\,1)$ plane. A CTB step and a partial dislocation are also shown at S and T, respectively. The inset is a simulated image calculated with experimental data. (b, c) The structural model of the $(1\,1\,0)\,[\frac{1}{2}0\frac{1}{2}]$ CSP as well as other defects projected along the $[1\bar{1}1]$ direction, and illustrated in the (0 1 0) layer structure, respectively. (d) The pattern of oxygen vacancies required to produce the $(1\,1\,0)\,[\frac{1}{2}0\frac{1}{2}]$ CSP shown in (c) by the operation of $(1\,1\,0)\,[\frac{1}{2}0\frac{1}{2}]$.

$[\frac{1}{2}0\frac{1}{2}]$. This operation is possible if one oxygen atom is eliminated from the (0 1 0) structure of the perfect structure. The pattern of the required vacant oxygen site is shown in Fig. 2h. Therefore, the CSP step can be regarded as being oxygen deficient as compared with the perfect structure.

Fig. 3a shows the HRTEM image of a crystallite viewed along the $[1\bar{1}1]$ direction. The image was taken under the defocus $\Delta f = -10$ nm which was measured by *in situ* Fourier transformation of amorphous SnO_2 existing at the edge of the sample. Bright spots in the micrograph correspond to projections of tin atoms along the $[1\bar{1}1]$ direction, which is supported by image simulation (inset). Except for the defocus of the objective lens, the parameters used for the inset in Fig. 3a are the same as those for the inset in Fig. 2a. The orientations of characteristic lattice planes associated with the viewing direction are marked. There is a CSP between S and T, oriented parallel to the (1 1 0) plane. Two (1 1 0) metal atomic planes at the CSP are much closer than common (1 1 0) metal atomic planes. Fig. 3b shows a possible structural model of this CSP, in which the relaxation of atoms at the CSP is neglected. Tin atoms belonging to the two closer tin planes at the CSP fill pairs of face-sharing octahedra. Face-shared octahedra projected along the $[1\bar{1}1]$ direction are similar to those outlined in Fig. 2f. Fig. 3c shows the (0 1 0) structure of the CSP parallel to the (1 1 0) plane. The trace of the CSP is marked between S and T. The displacement vector of the CPS is determined to be $[\frac{1}{2}0\frac{1}{2}]$. The octahedra containing the marked tin atoms at the CSP share faces with $[SnO_6]$ octahedra in the upper adjacent (0 1 0) layer. The CSP in Fig. 3c can be obtained by an operation of $(1\,1\,0)\,[\frac{1}{2}0\frac{1}{2}]$. Fig. 3d shows the pattern of the oxygen vacancies required by the operation. It suggests that the $(1\,1\,0)\,[\frac{1}{2}0\frac{1}{2}]$ CSP is also oxygen-deficient with respect to the perfect structure. Fig. 3 also shows the interaction between planar defects such as the $(1\,1\,0)\,[\frac{1}{2}0\frac{1}{2}]$ CSP, the $(\bar{1}\,0\,1)\,[\frac{1}{2}0\frac{1}{2}]$

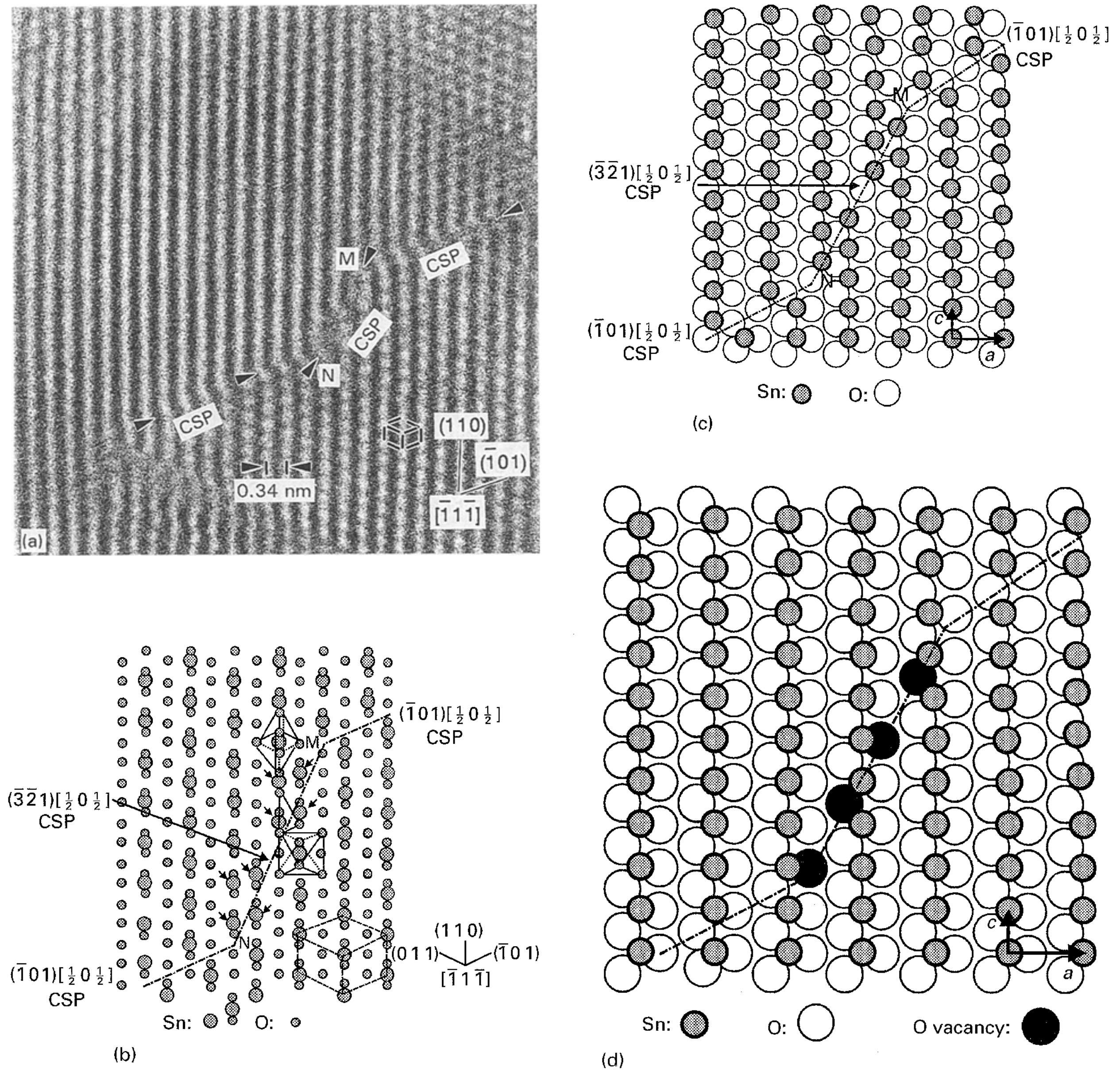

Figure 4 (a) HRTEM image of an SnO_2 crystallite taken along the $[\bar{1}1\bar{1}]$ direction, showing a $(\bar{3}\bar{2}1)$ $[\frac{1}{2}0\frac{1}{2}]$ CSP between M and N as well as $(\bar{1}01)$ $[\frac{1}{2}0\frac{1}{2}]$ CSPs. Partial dislocations due to the interaction between the CSPs are also shown at M and N, respectively. (b, c) The structural model of the $(\bar{3}\bar{2}1)$ $[\frac{1}{2}0\frac{1}{2}]$ CSP projected along the $[1\bar{1}1]$ direction, and illustrated in the (0 1 0) layer structure, respectively. (d) The pattern of oxygen vacancies required to produce the $(\bar{3}\bar{2}1)$ $[\frac{1}{2}0\frac{1}{2}]$ CSP shown in (c) by the operation of $(\bar{3}\bar{2}1)$ $[\frac{1}{2}0\frac{1}{2}]$.

CSP and coherent twin boundary (CTB). The interaction between the (1 1 0) $[\frac{1}{2}0\frac{1}{2}]$ CSP and the $(\bar{1}01)$ $[\frac{1}{2}0\frac{1}{2}]$ CSP results in a partial dislocation of Burgers vector $[\frac{1}{2}0\frac{1}{2}]$ at T. The partial dislocation is along the intersecting line of the CSPs, that is, along the $[1\bar{1}1]$ direction. The interaction between the (1 1 0) $[\frac{1}{2}0\frac{1}{2}]$ CSP and the CTB leads to the formation of a CTB step (at S). The CTB step is also oriented along the $[1\bar{1}1]$ direction.

Fig. 4a is the HRTEM image of a SnO_2 crystallite taken along the $[\bar{1}1\bar{1}]$ direction, showing a CSP between M and N. This CSP is parallel to the $(\bar{3}\bar{2}1)$ plane. A corresponding model projected along $[\bar{1}1\bar{1}]$ is shown in Fig. 4b. This model was made by an operation of $(\bar{3}\bar{2}1)$ $[\frac{1}{2}0\frac{1}{2}]$. It is consistent with the characteristics of the HRTEM image of the CSP. The marked pairs of tin atoms with a shorter distance in Fig. 4b are situated at the centres of the oxygen octahedra joined by face-sharing. Fig. 4c shows the (0 1 0) layer structure of the CSP. The trace of the CSP is represented by a dash-dot line between M and N. The pattern of oxygen vacant sites which are necessary to allow the operation $(\bar{3}\bar{2}1)$ $[\frac{1}{2}0\frac{1}{2}]$ is shown in Fig. 4d. Therefore, the Sn/O ratio at the $(\bar{3}\bar{2}1)$ $[\frac{1}{2}0\frac{1}{2}]$ CSP is higher than 1:2, the stoichiometric composition of perfect SnO_2. The interaction between the $(\bar{3}\bar{2}1)$ $\frac{1}{2}[101]$ CSP and the $(\bar{1}01)$ $[\frac{1}{2}0\frac{1}{2}]$ CSP is also shown in Fig. 4. Partial dislocations exist at their intersecting lines at M and N, respectively. The dislocations parallel to the $[\bar{1}1\bar{1}]$ direction have the Burgers vector of $[\frac{1}{2}0\frac{1}{2}]$.

4. Conclusion

HRTEM investigations of CSPs were carried out in nanometre-sized SnO_2 crystallites which nucleate and grow in amorphous oxygen-deficient SnO_{2-x} films when annealed in synthetic air at 700 °C for 1–2 h.

CSPs can be regarded as being oxygen deficient as compared with perfect SnO_2 when they are not parallel to their displacement vectors. The Sn/O ratio at CSP steps and at terminal places of CSPs is higher than that of the perfect structure. These defects are able to provide extra free electrons with the films.

Acknowledgement

This work was completed under the auspices of the BMFT project "Intelligent Gas Sensors" (contract 13MV0297).

References

1. S. SAMSON and C. G. FONSTED, *J. Appl. Phys.* **44** (1973) 4618.
2. Z. M. JARZEBSKI and J. P. MARTON, *J. Electrochem. Soc.* **123** (1976) 199c.
3. K. D. SCHIERBAUM, U. WEIMAR and W. GÖPEL, *Sensors Actuators* **B7** (1992) 709.
4. K. IHOKURA and J. WATSON, "The Stannic Oxide Gas Sensor-Principles and Applications" (CRC Press, Boca Raton, Ann Arbor, London, Tokyo, 1994).
5. "Tin Chemicals the Formula for Success", ITRI Publication 684 (John Swain, London, 1988) p. 5.
6. S. SUGANO, "Microcluster Physics" (Springer, Berlin, 1991).
7. W. A. de HEER, *Rev. Mod. Phys.* **65** (1993) 611.
8. K. D. SCHIERBAUM, U. WEIMAR and W. GÖPEL, *Sensors Actuators* **B3** (1991) 205.
9. C. Y. XIE, L. D. ZHANG, Z. G. ZHU, Y. HU, Z. Y. CHEN and X. M. WANG, *Chin. Sci. Bull.* (*China*) **37** (1992) 1790.
10. N. YAMAZOE, *Sensors Actuators* **B5** (1991) 7.
11. L. BRUNO, C. PIJOLAT and R. LALAUZE, *ibid* **B18-19** (1994) 195.
12. W. GÖPEL and K.D. SCHIERBAUM, *ibid.* **B26-27** (1995).
13. D. Z. WANG, S. L. WEN and J. CHEN, *Phys. Rev.* **B49** (1994) 14282.
14. J. C. H. SPENCE, "Experimental High-Resolution Electron Microscopy" (Clarendon Press, Oxford, 1981).
15. von H. W. BAUR, *Acta. Crystallogr.* **9** (1956) 515.

Received 31 May
and accepted 20 November 1995